

Riemannian Flow Matching on General Geometries

Ricky T. Q. Chen¹ Yaron Lipman^{1 2}

Abstract

We propose Riemannian Flow Matching (RFM), a simple yet powerful framework for training continuous normalizing flows on manifolds. Existing methods for generative modeling on manifolds either require expensive simulation, inherently cannot scale to high dimensions, or use approximations to limiting quantities that result in biased objectives. Riemannian Flow Matching bypasses these inconveniences and exhibits multiple benefits over prior approaches: It is completely simulation-free on simple geometries, it does not require divergence computation, and its target vector field is computed in closed form even on general geometries. The key ingredient behind RFM is the construction of a simple kernel function for defining per-sample vector fields, which subsumes existing Euclidean cases. Extending to general geometries, we rely on the use of spectral decompositions to efficiently compute kernel functions. Our method achieves state-of-the-art performance on real-world non-Euclidean datasets, and we showcase, for the first time, tractable training on general geometries, including on triangular meshes and maze-like manifolds with boundaries.

1. Introduction

While generative models have seen great advances recently for fitting data distributions residing on Euclidean spaces, dealing with data that naturally resides in some non-Euclidean space, *i.e.* a Riemannian manifold, still poses some challenges including scalability to high dimensions (*e.g.* Rozen et al. (2021)), the need for simulation or iterative sampling during training even for simple geometries such as hyperspheres (*e.g.* Mathieu & Nickel (2020); De Bortoli et al. (2022)), and difficulties in adapting to high-dimensional non-Euclidean manifolds.

In this work, we develop Riemannian Flow Matching

¹Meta AI (FAIR) ²Weizmann Institute of Science. Correspondence to: Ricky T. Q. Chen <rtqichen@meta.com>, Yaron Lipman <yaron.lipman@weizmann.ac.il>.

Preprint.

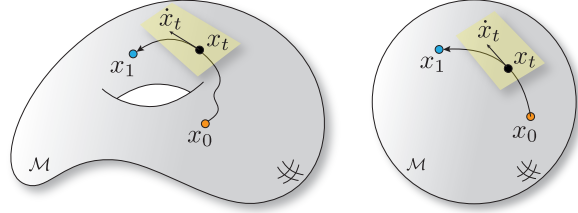


Figure 1: Riemannian Conditional Flow Matching (RCFM) regresses onto the vector field of flows x_t connecting a source $x_0 \sim p$ and a target $x_1 \sim q$. (Left) On general geometries, x_t is obtained through solving an ODE. (Right) On simple geometries (*e.g.*, hypersphere), RCFM can set x_t as a geodesic path and is completely simulation-free.

(RFM), a significant generalization of the recent Flow Matching approach (Lipman et al., 2023; Albergo & Vanden-Eijnden, 2023; Liu et al., 2023) to the manifold setting. RFM provides a very simple yet powerful methodology for learning continuous normalizing flows (CNFs; Chen et al. (2018)) on general Riemannian geometries \mathcal{M} .

Riemannian Flow Matching is built on top of the Flow Matching framework and learns a CNF by regressing an implicitly defined target vector field $u_t(x)$ pushing some base distribution p to a target distribution q that is defined by the training examples. To bypass the intractability of $u_t(x)$, we use a similar construction to Conditional Flow Matching and regress onto conditional vector fields, $u_t(x|x_1)$, pushing p to a *single* training example, x_1 .

A key observation behind our Riemannian generalization is that such a conditional vector field, required for training the CNF, can be written explicitly in terms of a positive *kernel function* $k(x, y) > 0$ that discriminates pairs of points x, y on the manifold. One natural choice for such a kernel is the geodesic distance function $d_g(x, y)$, which coincides with straight trajectories used previously in Euclidean space.

On simple geometries where geodesics are known in closed form (*e.g.* Euclidean space, hypersphere, hyperbolic space, torus, any of their product spaces), Riemannian Flow Matching remains **completely simulation-free**. Even on general geometries, it only requires forward simulation of a relatively simple ordinary differential equation (ODE), *i.e.*, no

differentiation through the solver, no stochastic iterative sampling, and no divergence estimation are needed.

On all types of geometries, Riemannian Flow Matching exhibits several advantages over recently proposed Riemannian diffusion models (De Bortoli et al., 2022; Huang et al., 2022) which require: (i) iterative simulation of a noising process during training even for geometries that possess analytic geodesic formulas; (ii) approximations of either score functions or (iii) divergences of the parametric vector field; and (iv) solving stochastic differential equations (SDE) which generally is harder to approximate than ODE solutions (Kloeden et al., 2002). Table 1 summarizes some key differences to relevant prior methods.

We empirically find that Riemannian Flow Matching achieves state-of-the-art performance on manifold datasets in almost all settings compared to the most competitive baselines. We also show that our approach can scale to higher dimensions with no loss in performance on the simple geometries considered by prior works. Furthermore, we show for the first time, the tractable training of continuous-time deep generative models that lie on non-trivial geometries including those imposed by discrete triangular meshes, and manifolds with non-trivial boundaries representing hard constraints on maze-shaped manifolds.

2. Preliminaries

Riemannian manifolds. This paper considers connected and compact Riemannian manifolds \mathcal{M} with metric g as basic domain over which the generative model is learned. Tangent space to \mathcal{M} at $x \in \mathcal{M}$ is denoted $T_x\mathcal{M}$, and g defines an inner product over $T_x\mathcal{M}$ denoted $\langle u, v \rangle_g$, $u, v \in T_x\mathcal{M}$. $T\mathcal{M} = \cup_{x \in \mathcal{M}} \{x\} \times T_x\mathcal{M}$ is the tangent bundle that collects all the tangent planes of the manifold. $\mathfrak{U} = \{u_t\}$ denotes the space of time dependent smooth vector fields (VFs) $u : \mathcal{M} \rightarrow T\mathcal{M}$, where $u_t(x) \in T_x\mathcal{M}$ for all $x \in \mathcal{M}$. We will denote by $d\text{vol}_x$ the volume element over \mathcal{M} , and integration of a function $f : \mathcal{M} \rightarrow \mathbb{R}$ over \mathcal{M} is denoted $\int f(x)d\text{vol}_x$.

Probability paths and flows on manifolds. Probability densities over \mathcal{M} are continuous non-negative functions $p : \mathcal{M} \rightarrow \mathbb{R}_+$, so that $\int p(x)d\text{vol}_x = 1$. The space of probability densities over \mathcal{M} is marked $\mathfrak{P} = \{p\}$. A *probability path* p_t is a curve in probability space $p_t : [0, 1] \rightarrow \mathfrak{P}$; such paths will be used to supervise the generative models. A flow defines a diffeomorphism $\Psi : \mathcal{M} \rightarrow \mathcal{M}$ by integrating instantaneous deformations represented by a time-dependent vector field $u_t \in \mathfrak{U}$. Specifically, a time-dependent flow, $\psi_t : \mathcal{M} \rightarrow \mathcal{M}$, is defined as solving the following ordinary

	Simulation-free on simple geo.	Closed-form conditional	Does not require divergence
Ben-Hamu et al. (2022)	✓	—	✗
De Bortoli et al. (2022) (DSM)	✗	✗	✓
De Bortoli et al. (2022) (ISM)	✗	—	✗
Huang et al. (2022)	✗	—	✗
Riemannian FM (<i>Ours</i>)	✓	✓	✓

Table 1: Comparison of closely related methods for training continuous-time generative models on Riemannian manifolds. Additionally, we are the only among these works to consider and tackle general geometries.

differential equation (ODE) on \mathcal{M} over $t \in [0, 1]$,

$$\begin{aligned} \frac{d}{dt}\psi_t(x_0) &= u_t(\psi_t(x_0)), \\ \psi_0(x_0) &= x_0, \end{aligned} \quad (1)$$

and the final diffeomorphism is defined by setting $\Psi(x_0) = \psi_1(x_0)$. Given a probability density path p_t , it is said to be *generated* by u_t from p if

$$p_t(x) = ([\psi_t]_{\#}p)(x) = p(\psi_t^{-1}(x))e^{-\int_0^t \text{div}(u_s)(x_s)ds} \quad (2)$$

where the $\#$ symbol denotes the standard push-forward operation and $x_s = \psi_s(\psi_t^{-1}(x))$. Previously, Chen et al. (2018) suggested modeling the flow ψ_t implicitly by considering parameterizing the vector field u_t . This results in a deep generative model of the flow ψ_t , called a *Continuous Normalizing Flow* (CNF) which models a probability path p_t through a continuous-time deformation of a base distribution p . A number of works have formulated manifold variants (Mathieu & Nickel, 2020; Lou et al., 2020; Falorsi, 2020) that require simulation in order to enable training, while existing simulation-free variants (Rozen et al., 2021; Ben-Hamu et al., 2022) scale poorly to high dimensions and do not adapt to general geometries.

3. Method

We aim to train a generative model that lie on a smooth, compact Riemannian manifold \mathcal{M} endowed with a metric g . Concretely, we are given a set of training samples x_1 from some unknown data distribution $q(x_1)$ lying on \mathcal{M} . Our goal is to find a map $\Phi : \mathcal{M} \rightarrow \mathcal{M}$ that pushes p (some simple base distribution) to q at exactly time $t = 1$.

3.1. Flow Matching on Manifolds

We first make the necessary adaption to formulate Flow Matching on Riemannian manifolds. Derivations of the manifold case with full details are placed in Appendix A. Flow Matching (Lipman et al., 2023) is a method to train Continuous Normalizing Flow (CNF) on Euclidean space that sidesteps likelihood computation during training and

scales extremely well, similar to diffusion models (Ho et al., 2020; Song et al., 2020b) that use simple noise processes.

Riemannian Flow Matching. Flow Matching (FM) trains a CNF by fitting a parametric vector field $v_t(x)$, with parameters $\theta \in \mathbb{R}^p$, to an *a priori* defined vector field $u_t(x)$ that generates a desired probability density path $p_t(x)$ over \mathcal{M} satisfying $p_{t=0}(x) = p$ and $p_{t=1}(x) = q(x)$. On a manifold endowed with a Riemannian metric g , the Flow Matching objective takes the form

$$\mathcal{L}_{\text{RFM}}(\theta) = \mathbb{E}_{t, p_t(x)} \|v_t(x) - u_t(x)\|_g^2 \quad (3)$$

where $t \sim \mathcal{U}[0, 1]$, the uniform distribution over $[0, 1]$. Note that both $u_t(x)$ and $v_t(x)$ belong to the tangent space $T_x\mathcal{M}$ of \mathcal{M} at x and are compared using the Riemannian metric g over that tangent space.

Probability path construction. Training Flow Matching therefore requires coming up with a probability density path p_t , $t \in [0, 1]$, satisfying the boundary conditions

$$p_0 = p, \quad p_1 = q \quad (4)$$

and a corresponding VF u_t generating p_t from p in the sense of equation 2. One way to construct such a pair is choosing p_t to be a *marginal probability path*, i.e. of the form

$$p_t(x) = \int_{\mathcal{M}} p_t(x|x_1)q(x_1)d\text{vol}_{x_1} \quad (5)$$

and $p_t(x|x_1)$ is a conditional probability path satisfying

$$p_0(x|x_1) = p(x), \quad p_1(x|x_1) \approx \delta_{x_1}(x), \quad (6)$$

where $\delta_{x_1}(x)$ is the Dirac distribution over \mathcal{M} centered at x_1 . In this case, a marginal vector field that generates the marginal p_t is given by the formula

$$u_t(x) = \int_{\mathcal{M}} u_t(x|x_1) \frac{p_t(x|x_1)q(x_1)}{p_t(x)} d\text{vol}_{x_1} \quad (7)$$

Unfortunately, computing this u_t is intractable as it requires marginalizing over the entire data distribution q .

Riemannian Conditional Flow Matching. A key insight from Lipman et al. (2023) is that when the targets p_t and u_t are defined as in equations 5 and 7, FM is equivalent to the following Conditional Flow Matching objective,

$$\mathcal{L}_{\text{RCFM}}(\theta) = \mathbb{E}_{t, q(x_1), p_t(x|x_1)} \|v_t(x) - u_t(x|x_1)\|_g^2 \quad (8)$$

as long as $u_t(x|x_1)$ is a vector field that generates $p_t(x|x_1)$ from p . To further simplify this RCFM loss, we denote by $\psi_t(x_0|x_1)$ the flow solution of the ODE in equation 1 with $u_t(x_0|x_1)$ and initial condition $\psi_0(x_0|x_1) = x_0$.

Since $u_t(x|x_1)$ generates $p_t(x|x_1)$ from $p(x_0)$, we can reparameterize the sample from $p_t(x|x_1)$ in terms of x_0 and express equation 8 as

Algorithm 1 Riemannian Flow Matching

Require: base distribution p , training examples $x_1 \sim q$

Initialize parameters θ of v_t

while not converged **do**

sample time $t_* \sim \mathcal{U}(0, 1)$

sample noise $x_0 \sim p$

sample training example $x_1 \sim q$

if simple geometry **then**

$x_t = \exp_{x_0}(t \log_{x_0}(x_1))$

else if general geometry **then**

$x_t = \text{solve_ODE}([0, t_*], x_0, u_t(x|x_1))$

end if

$\ell(\theta) = \|v_t(x_t; \theta) - \dot{x}_t\|_g^2$

$\theta = \text{optimizer_step}(\ell(\theta))$

end while

$$\mathcal{L}_{\text{RCFM}}(\theta) = \mathbb{E}_{t, q(x_1), p(x_0)} \|v_t(x_t) - \dot{x}_t\|_g^2 \quad (9)$$

where $\dot{x}_t = d/dt x_t$ and we define the shorthand

$$x_t = \psi_t(x_0|x_1). \quad (10)$$

This is the general manifold analog of Conditional Flow Matching (Lipman et al., 2023). In the general case, for every data point $x_1 \sim q$, we solve the ODE in equation 1 with the conditional VF $u_t(x|x_1)$ starting with a random initial condition $x_0 \sim p$ to get the path x_t , then optimize equation 9. See Figure 1 for an illustration of the training process, and Algorithm 1 for its pseudo-code.

The crucial remaining component for Riemannian Flow Matching is therefore:

Can we construct computationally tractable conditional VFs $u_t(x|x_1)$ on general manifolds so that their generated probability paths $p_t(x|x_1)$ satisfy the desired boundary conditions in equation 6?

This question is answered positively next.

3.2. Constructing Conditional Vector Fields

We construct conditional VFs $u_t(x|x_1)$ such that generated probability paths $p_t(x|x_1)$ will concentrate all the mass at x_1 at time $t = 1$, i.e. satisfying equation 6. To that end we make use a *kernel function* $k : \mathcal{M} \times \mathcal{M} \rightarrow \mathbb{R}$, defined as satisfying the following properties:

1. *Non-negative:* $k(x, y) \geq 0$ for all $x, y \in \mathcal{M}$.
2. *Positive:* $k(x, y) \neq 0$ iff $x \neq y$.
3. *Non-degenerate:* $\nabla k(x, y) = 0$ iff $x = y$.

We use as convention $\nabla k(x, y) = \nabla_x k(x, y)$. Given such a kernel function we define the conditional vector field to be

$$u_t(x|x_1) = -\frac{k(x, x_1)}{1-t} \frac{\nabla k(x, x_1)}{\|\nabla k(x, x_1)\|_g^2} \quad (11)$$

The non-degenerate property of the kernel k guarantees this vector-field is defined everywhere except when $x = x_1$.

The motivation behind this definition is that this VF transports all points $x \in \mathcal{M}$ from $t = 0$ to x_1 at time $t = 1$:

Proposition 3.1. *The flow $\psi_t(x_0|x_1)$ defined by the vector field in equation 11 satisfies*

$$k(\psi_t(x_0|x_1), x_1) = (1-t)k(x_0, x_1) \quad (12)$$

Proof. Differentiating the time-dependent scalar function $k(\psi_t(x_0|x_1), x_1)$ w.r.t. t , and denoting $x_t = \psi_t(x_0|x_1)$,

$$\begin{aligned} \frac{d}{dt} k(x_t, x_1) &= \left\langle \nabla k(x_t, x_1), \frac{dx_t}{dt} \right\rangle_g \\ &= \langle \nabla k(x_t, x_1), u_t(x_t|x_1) \rangle_g \\ &= -\frac{k(x_t, x_1)}{1-t} \end{aligned}$$

Solutions to this ODE are of the form $k(x_t, x_1) = c(1-t)$, where $c > 0$ is a constant set by the initial conditions. Noting that $k(x_t, x_1) = k(x_0, x_1)$ at $t = 0$ sets $c = k(x_0, x_1)$, and the proposition is proved. \square

A direct consequence of Proposition 3.1 is that the conditional probability path generated by the VF $u_t(x|x_1)$ in equation 11 satisfies the desired boundary conditions in equation 6. To see this, take any $x_0 \neq x_1$, let $x_t = \psi_t(x_0|x_1)$, then due to the non-negativity and the positivity properties of the kernel, we know that $k(x_t, x_1) > 0$ for $t \in [0, 1)$ and is linearly decreasing to zero. At time $t = 1$, it reaches exactly zero. Thus we have $p_1 = \psi_1(\cdot|x_1)_{\#} p = \delta_{x_1}$, satisfying the boundary conditions. Simply speaking, the flow generated by the conditional VF $u_t(x|x_1)$ is linearly decreasing the positive kernel function for all points $x \neq x_1$ until all points synchronously reach x_1 at time $t = 1$; Figure 2 provides an illustration.

Plugging this conditional VF into the RCFM objective (9) and using equation 12, we arrive at a more explicit form,

$$\mathcal{L}_{\text{RCFM}}(\theta) = \mathbb{E}_{t, q(x_1)} \left\| v_t(x_t) + k(x_0, x_1) \frac{\nabla k(x_t, x_1)}{\|\nabla k(x_t, x_1)\|_g^2} \right\|_g^2.$$

Although for general manifolds \mathcal{M} and kernel functions k , training with Riemannian CFM requires simulation of an ODE to get x_t , it does not need to backprop through x_t . Moreover, as we shall show next, on simple geometries, RCFM is completely simulation-free by using the geodesic distance as the kernel function.

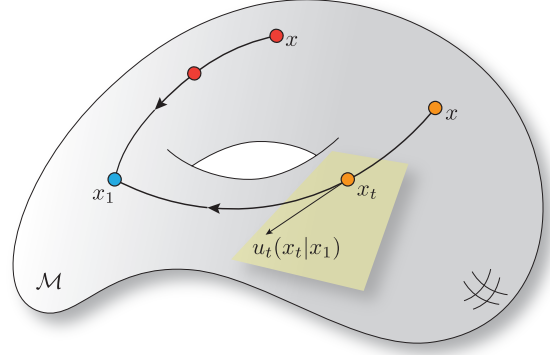


Figure 2: The conditional vector field $u_t(x|x_1)$ in equation 11 transports all points $x \neq x_1$ to x_1 at exactly time $t = 1$.

Geodesic distance. A natural choice for the kernel function $k(x, y)$ over a Riemannian manifold \mathcal{M} is the geodesic distance $d_g(x, y)$, which is defined by the shortest path connecting x and y in \mathcal{M} :

$$d_g(x, y) = \inf \left\{ \int_0^1 \|\dot{\gamma}(t)\|_g dt \mid \gamma: [0, 1] \rightarrow \mathcal{M}, \gamma(0)=x, \gamma(1)=y \right\}. \quad (13)$$

We first note that when using geodesic distance as the kernel function, the flow $x_t = \psi_t(x_0|x_1)$ in equation 10 becomes a geodesic path connecting x_0 and x_1 .

Proposition 3.2. *Consider a compact and smooth Riemannian manifold \mathcal{M} and metric g with geodesic distance $d_g(x, y)$. In case $k(x, y) = d_g(x, y)$ then $x_t = \psi_t(x_0|x_1)$ defined in equation 10 with the conditional VF in equation 11 is a geodesic connecting x_0 to x_1 .*

The proof can be found in Appendix B. On simple geometries—such as Euclidean space, the hypersphere, hyperbolic space, and the high-dimensional torus—an analytical formula is known for computing geodesics connecting pairs of points. In particular, the geodesic connecting x_0 and x_1 can be expressed in terms of the exponential and logarithm maps,

$$x_t = \exp_{x_0}(t \log_{x_0}(x_1)). \quad (14)$$

This formula can simply be plugged into equation 9. Figure 1 (Right) shows an illustration for a sphere where x_t is computed exactly in closed form.

Euclidean geometry. With Euclidean geometry $\mathcal{M} = \mathbb{R}^n$, and with standard Euclidean norm $d(x, y) = \|x - y\|_2$, the conditional VF (equation 11) reduces to

$$u_t(x|x_1) = \frac{x_1 - x}{1-t},$$

and the RCFM objective takes the form

$$\mathcal{L}_{\text{RCFM}}(\theta) = \mathbb{E}_{t, q(x_1), p(x_0)} \|v_t(x_t) + x_0 - x_1\|_2^2,$$

which coincides with the Euclidean case of Flow Matching with straight paths presented in prior works (Lipman et al., 2023; Albergo & Vanden-Eijnden, 2023; Liu et al., 2023), demonstrating that these are special cases of Riemannian Flow Matching when using geodesic paths.

3.3. Spectral Distances on General Geometries

For general geometries, the geodesic distance can be difficult to compute efficiently, especially since training requires repeatedly computing this for any possible pair of points. We thus propose the use of distance metrics that can be computed quickly for any pair of points on \mathcal{M} contingent on a one-time preprocessing step.

In particular, for general Riemannian manifolds, we consider the use of spectral distances as an alternative to the geodesic distance. Additionally, spectral distances offer some benefits over the geodesic distance such as robustness to topological noise, smoothness, and are globally geometry-aware (Lipman et al., 2010).

Let $\varphi_i : \mathcal{M} \rightarrow \mathbb{R}$ be the eigenfunctions of the Laplace-Beltrami operator Δ_g over \mathcal{M} with corresponding eigenvalues λ_i , i.e. they satisfy

$$\Delta_g \varphi_i = \lambda_i \varphi_i, \quad i = 1, 2, \dots$$

then spectral distances are of the form

$$d_w(x, y)^2 = \sum_{i=1}^{\infty} w(\lambda_i) (\varphi_i(x) - \varphi_i(y))^2, \quad (15)$$

where $w : \mathbb{R} \rightarrow \mathbb{R}_+$ is some monotonically decreasing weighting function. Popular instances of spectral distances include:

1. *Diffusion Distance* (Coifman & Lafon, 2006)
 $w(\lambda) = \exp(-2\tau\lambda)$, with a hyperparameter τ .
2. *Biharmonic Distance* (Lipman et al., 2010)
 $w(\lambda) = \lambda^{-2}$.

In practice, spectral distances are often computed by truncating the infinite series in equation 15, and using only k eigenvectors corresponding to the smallest k eigenvalues (i.e., the dominant terms in the sum, excluding the first eigenvalue which is zero). Figure 8 shows contour plots of these spectral distances for general manifolds.

Computation cost. The smallest k eigenvalues and their eigenfunctions need only be computed once as a preprocessing step. Afterwards, spectral distances can be computed very efficiently for all pairs of points. Note however, that training with RCFM does still require solving for x_t , but as the vector fields (equation 11) are simple and cheap to evaluate, the flows can be computed efficiently.

Sufficiency with finite k . One may wonder if we pay any approximation costs when using finite k ; the answer is no. In fact, we only need as many eigenfunctions as it takes to be able to distinguish (almost) every pair of points on the manifold. Put differently, we don't need to compute the spectral distances perfectly, only sufficiently enough that the conditions of our kernel function are satisfied. Regarding the question of what k is enough? This is only understood partially: for local neighborhoods the number of required eigenfunctions is the manifold dimension (but not necessarily the first ones), a property proven in (Jones et al., 2008, Theorem 2). Nevertheless, the use of spectral distances computed with k smallest eigenvectors is equivalent to computing Euclidean distances in a k -dimensional Euclidean embedding using the same eigenfunctions; this embedding is known to preserve neighborhoods optimally (Belkin & Niyogi, 2003).

3.4. Manifolds with Boundary

In considering general geometries, we also consider the case where \mathcal{M} has a boundary, denoted $\partial\mathcal{M}$. In this case, we need to add another condition to our kernel to make sure $u_t(x|x_1)$ will not flow particles outside the manifold. Let $n(x) \in T_x\mathcal{M}$ denote the interior-pointing normal direction at a boundary point $x \in \partial\mathcal{M}$. We add the following condition to our kernel function:

$$4. \text{ Boundary: } \langle \nabla k(x, y), n(x) \rangle_g \leq 0, \quad \forall y \in \mathcal{M}, x \in \partial\mathcal{M}.$$

If the kernel function satisfies this condition, then the conditional VF in equation 11 satisfies

$$\langle u_t(x|x_1), n(x) \rangle_g \geq 0$$

implying that the conditional vector field does not point outwards on the boundary of the manifold.

Spectral distances at boundary points. In case \mathcal{M} has boundary we want to make sure the spectral distances in equation 15 satisfy the boundary condition. To ensure this, we can simply solve eigenfunctions φ_i using the natural, or Neumann, boundary conditions, i.e., their normal derivative at boundary points vanish, and we have $\langle \nabla_g \varphi_i(x), n(x) \rangle_g = 0$ for all $x \in \partial\mathcal{M}$. This property implies that $\langle \nabla_x d_w(x, y)^2, n(x) \rangle_g = 0$, satisfying the boundary condition of the kernel.

4. Related Work

Deep generative models on Riemannian manifolds have been studied previously. First few works suggested constructing normalizing flows that map between simple manifolds and an Euclidean space of the same intrinsic dimension

Table 2: Test NLL on Earth and climate science datasets. Standard deviation estimated over 5 runs.

	Volcano	Earthquake	Flood	Fire
Dataset size (train + val + test)	827	6120	4875	12809
<i>CNF-based</i>				
Riemannian CNF (Mathieu & Nickel, 2020)	-6.05±0.61	0.14±0.23	1.11±0.19	-0.80±0.54
Moser Flow (Rozen et al., 2021)	-4.21±0.17	-0.16±0.06	0.57±0.10	-1.28±0.05
CNF Matching (Ben-Hamu et al., 2022)	-2.38±0.17	-0.38±0.01	0.25±0.02	-1.40±0.02
Riemannian Score-Based (De Bortoli et al., 2022)	-4.92±0.25	-0.19±0.07	0.48±0.17	-1.33±0.06
<i>ELBO-based</i>				
Riemannian Diffusion Model (Huang et al., 2022)	-6.61±0.96	-0.40 ±0.05	0.43±0.07	-1.38±0.05
<i>Ours</i>				
Riemannian Flow Matching ^{w/} Geodesic	-7.93 ±1.67	-0.28±0.08	0.42 ±0.05	-1.86 ±0.11

(Gemici et al., 2016; Rezende et al., 2020; Bose et al., 2020), often relying on the tangent space at some pre-specified origin. However, this approach is problematic when the manifold is not homeomorphic to Euclidean space, resulting in both theoretical and numerical issues. On the other hand, continuous-time models such as continuous normalizing flows bypass such topological constraints and flow directly on the manifold itself. To this end, a number of works have formulated continuous normalizing flows on simple manifolds (Mathieu & Nickel, 2020; Lou et al., 2020; Falorsi, 2020), but these rely on maximum likelihood for training, a costly simulation-based procedure. More recently, simulation-free training methods for continuous normalizing flows on manifolds have been proposed (Rozen et al., 2021; Ben-Hamu et al., 2022); however, these scale poorly to high dimensions and do not adapt to general geometries. Another direction is when the manifold is unknown but assumed to be embedded in an ambient Euclidean space, works have discussed methods for learning the manifold directly (Brehmer & Cranmer, 2020; Kim et al., 2020; Horvat & Pfister, 2021).

With the influx of diffusion models that allow simulation-free training on Euclidean space (Ho et al., 2020; Song et al., 2020b), multiple works have attempted to adopt diffusion models to manifolds (Mathieu & Nickel, 2020; Huang et al., 2022). However, due to the use stochastic differential equations (SDE) and denoising score matching (Vincent, 2011), these approaches have inherently undesirable properties. First and foremost, they lose the simulation-free aspect that is offered in the Euclidean regime; this is because there is no manifold analog of the Ornstein–Uhlenbeck process—a simple SDE with closed form solutions. Hence, diffusion-based methods have to resort to simulated random walks as a noising process on even simple manifolds. Furthermore, even on simple manifolds, the conditional score function is not known analytically, so De Bortoli et al. (2022) proposed eigenfunction-based approximations but these ultimately lead to biased training gradients—in contrast, our approximation of the spectral distances is sufficient for finite k . A way to bypass the conditional score function is to use

implicit score matching (Hyvärinen & Dayan, 2005), which Huang et al. (2022) adopts for the manifold case, but this instead requires divergence computation during training. Using the Hutchinson estimator (Hutchinson, 1989; Skilling, 1989) for divergence estimation results in a more scalable algorithm (Song et al., 2020a), but the variance of Hutchinson scales poorly with dimension (Hutchinson, 1989). Finally, the use of SDEs requires carefully constructing suitable reverse-time processes that approximate either the probability path (Anderson, 1982) or the sample trajectories (Li et al., 2020), whereas ODE solutions are generally well-defined in both forward and reverse directions (Murray & Miller, 2013). In contrast to these methods, Riemannian Flow Matching is simulation-free on simple geometries, has exact conditional vector fields on all geometries, and does not require divergence computation. These properties have been summarized in Table 1.

Riemannian Flow Matching is built on top of recent simulation-free methods that work with ODEs instead of SDEs, regressing directly onto generating vector fields instead of score functions (Lipman et al., 2023; Albergo & Vanden-Eijnden, 2023; Liu et al., 2023; Neklyudov et al., 2022), resulting in an arguably simpler approach to continuous-time generative modeling without the need for stochastic differential equations. In particular, Lipman et al. (2023) shows that this approach encompasses and broadens the probability paths used by diffusion models while remaining simulation-free, Albergo & Vanden-Eijnden (2023) discusses an interpretation based on the use of interpolants—equivalent to our use of flows, Liu et al. (2023) shows that repeatedly fitting to a model’s own samples leads to straighter trajectories, and Neklyudov et al. (2022) formulates a variational objective when $u_t(x)$ is taken to be a gradient field.

5. Experiments

We empirically validate our approach on both synthetic and real-world datasets that lie naturally on a Riemannian manifold. We consider data from earth and climate science, pro-

Table 3: Test NLL on protein datasets. Standard deviation estimated over 5 runs.

	General (2D)	Glycine (2D)	Proline (2D)	Pre-Pro (2D)	RNA (7D)
Dataset size (train + val + test)	138208	13283	7634	6910	9478
Mixture of Power Spherical (Huang et al., 2022)	1.15 ± 0.002	2.08 ± 0.009	0.27 ± 0.008	1.34 ± 0.019	4.08 ± 0.368
Riemannian Diffusion Model (Huang et al., 2022)	1.04 ± 0.012	1.97 ± 0.012	0.12 ± 0.011	1.24 ± 0.004	-3.70 ± 0.592
Riemannian Flow Matching ^{w/} Geodesic	1.01 ± 0.025	1.90 ± 0.055	0.15 ± 0.027	1.18 ± 0.055	-5.20 ± 0.067

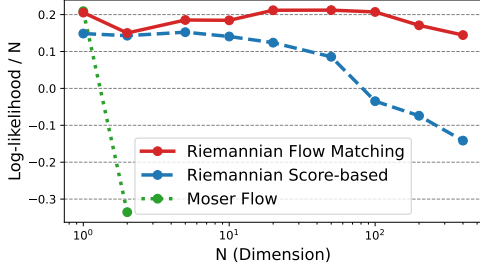


Figure 3: Riemannian Flow Matching scales incredibly well to higher dimensions as it is simulation-free and all quantities required for training are computed exactly on simple geometries. Log-likelihoods are in bits.

tein structures, high-dimensional tori, complicated synthetic distributions on general closed manifolds, and distributions on maze-shaped manifolds that require navigation across non-trivial boundaries. Details regarding training setups and numerical solver schemes are discussed in Appendix D.

5.1. Earth and Climate Science Datasets on the Sphere

We make use of the publicly sourced datasets (NOAA, 2020a;b; Brakenridge, 2017; EOSDIS, 2020) compiled by Mathieu & Nickel (2020). These data points lie on the 2-D sphere, a simple manifold with closed form exponential and logarithm maps. We therefore stick to the geodesic distance and compute geodesics in closed form as in equation 14.

Table 2 shows the mean and standard deviation of negative log likelihood (NLL) on the test set computed over 5 random runs with different splits of the dataset, as was done in prior works. We achieve a sizable improvement on prior works on the volcano and fire datasets which have highly concentrated regions that require a high fidelity. We also plot the density of our trained models in Figure 6.

5.2. Protein Datasets on the Torus

We make use of the preprocessed protein (Lovell et al., 2003) and RNA (Murray et al., 2003) datasets compiled by Huang et al. (2022). These datasets represent torsion angles and can be represented on the 2D and 7D torus. We represent the data on a flat torus, which is isometric to the product of 1-D spheres used by prior works (Huang et al., 2022;

Table 4: Test NLL on mesh datasets.

	Stanford Bunny			Spot the Cow		
	$k=10$	$k=50$	$k=100$	$k=10$	$k=50$	$k=100$
Riemannian Flow Matching						
^{w/} Diffusion ($\tau=1/4$)	1.16 ± 0.02	1.48 ± 0.01	1.53 ± 0.01	0.87 ± 0.07	0.95 ± 0.16	1.08 ± 0.05
^{w/} Biharmonic	1.06 ± 0.05	1.55 ± 0.01	1.49 ± 0.01	1.02 ± 0.06	1.08 ± 0.05	1.29 ± 0.05

De Bortoli et al., 2022) and have densities that are directly comparable due to this isometry.

Table 3 contains results aggregated over 5 random splits of the dataset. We match the performance of Huang et al. (2022) on the 2D tori as these models are likely close to optimal already. However, we see a significant gain in performance on the higher dimensional 7D torus, due to the higher complexity of the dataset. We show learned densities of the protein datasets in Figure 7.

5.3. High-Dimensional Tori

We consider the scalability of our method in the case of high-dimensional tori. Following the exact setup in (De Bortoli et al., 2022), we construct a wrapped Gaussian distribution on the N-D torus with a uniformly sampled mean and fixed variance of 0.2. We compare to Moser Flow (Rozen et al., 2021), which does not scale well into high dimensions, and Riemannian Score-based (De Bortoli et al., 2022) using their sliced score matching objective. As shown in Table 1, while this objective gets around the need to estimate conditional score functions, it requires stochastic divergence computation during training, introducing larger amounts of variance at higher dimensions. In Figure 3 we plot the test log-likelihood values, normalized by dimension, across these two baselines and our method with the geodesic construction. We see that our method performs steadily, with no significant drop in performance at higher dimensions since we do not have any stochastic estimation or reliance on approximations.

5.4. General Closed Manifolds

We next experiment with general closed manifolds using spectral distances as kernel functions as described in Section 3.3. Specifically, we experiment on manifolds described by triangular meshes, where computing eigenfunctions of the Laplace-Beltrami operator amounts to eigendecomposi-

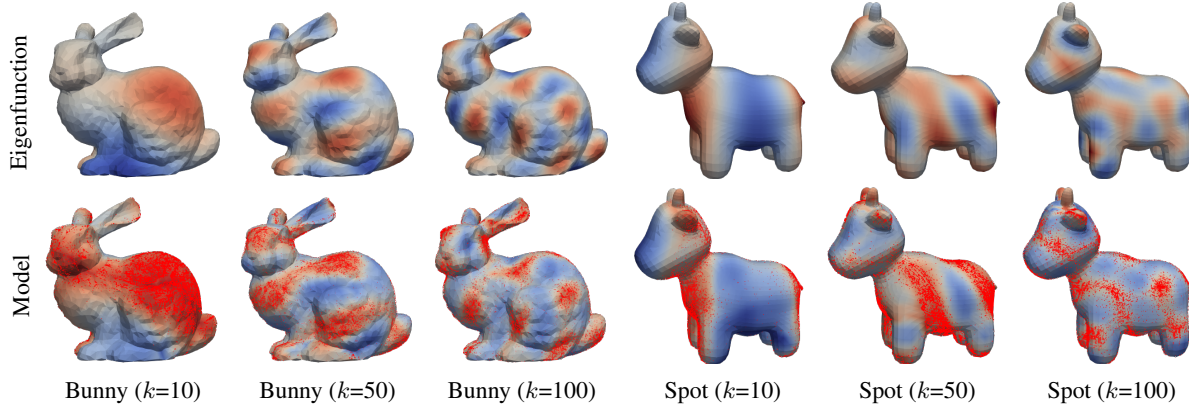


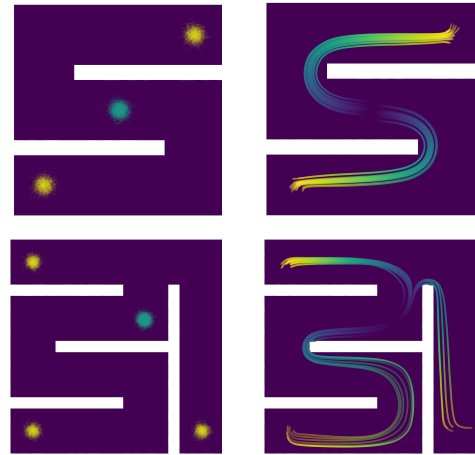
Figure 4: Visualization of the eigenfunctions that were used to construct target distributions, and the learned density & samples from trained models through Riemannian Flow Matching with the Biharmonic distance as kernel function.

tion of a sparse positive definite matrix, which can be done on the CPU rather efficiently. As our manifolds, we use the Standard Bunny (Laboratory) and Spot the Cow (Crane). We then construct synthetic distributions by computing the k -th eigenfunction, thresholding, and then sampling proportionally to the eigenfunction. This is done on an upsampled version of the mesh so that the distribution is not uniform on each triangle.

Figure 4 contains visualizations of the eigenfunctions, the learned density, and samples from a train model that transports from a uniform base distribution. We used $k=200$ eigenfunctions to compute spectral distances. Our method is able to produce high fidelity samples on these discrete mesh manifolds. In Section 5.3, we report the test NLL of models trained using either the diffusion distance or the biharmonic distance. We had to tune the diffusion distance hyperparameter τ while the biharmonic distance was straightforward to use as it has better smoothness properties (see Figure 8).

5.5. Manifolds with Boundary

Lastly, we experiment with manifolds that have boundaries. Specifically, we consider randomly generated mazes visualized in Figure 5a where walls in the maze are treated as uncrossable boundaries. We set the base distribution to be a Gaussian in the middle of the maze, and set the target distribution to be a mixture of densities at corners of the maze. These mazes are represented using triangular meshes, and we approximate the biharmonic distance using $k=30$ eigenfunctions. Once trained, the model represents a single vector field that transports all mass from the source distribution to the target distribution with no crossing paths. We plot sample trajectories in Figure 5b, where it can be seen that the learned vector field avoids boundaries of the manifold and successfully navigates the mazes.



(a) Distributions (b) Model trajectories

Figure 5: (a) Source (green) and target (yellow) distributions on a manifold with non-trivial boundaries. (b) Samples from a CNF model trained through Riemannian Flow Matching with the Biharmonic distance.

6. Conclusion

We propose Riemannian Flow Matching as a highly-scalable approach for training continuous normalizing flows on manifolds with general geometries. Our method bypasses many of the inherent inconveniences in prior methods, is completely simulation-free on simple geometries that have closed form geodesics, and applies readily to general geometries contingent on a one-time preprocessing cost. We find that our approach achieves state-of-the-art performance on real-world manifold datasets, with no drop in performance when scaling to high dimensions, and we showcase for the first time, tractable training on general geometries including both closed manifolds and manifolds with boundaries.

Acknowledgements

Ricky T. Q. Chen would like to thank Chin-Wei Huang for his help in clarifying his prior works. Additionally, we acknowledge the Python community (Van Rossum & Drake Jr, 1995; Oliphant, 2007) for developing the core set of tools that enabled this work, including PyTorch (Paszke et al., 2019), PyTorch Lightning (Falcon & team, 2019), Hydra (Yadan, 2019), Jupyter (Kluyver et al., 2016), Matplotlib (Hunter, 2007), seaborn (Waskom et al., 2018), numpy (Oliphant, 2006; Van Der Walt et al., 2011), SciPy (Jones et al., 2014) pandas (McKinney, 2012), geopandas (Jordahl et al., 2020), torchdiffeq (Chen, 2018), libigl (Panozzo & Jacobson, 2014), and PyEVTk (Herrera, 2019).

References

- Albergo, M. S. and Vanden-Eijnden, E. Building normalizing flows with stochastic interpolants. *International Conference on Learning Representations*, 2023.
- Anderson, B. D. Reverse-time diffusion equation models. *Stochastic Processes and their Applications*, 12(3):313–326, 1982.
- Belkin, M. and Niyogi, P. Laplacian eigenmaps for dimensionality reduction and data representation. *Neural computation*, 15(6):1373–1396, 2003.
- Ben-Hamu, H., Cohen, S., Bose, J., Amos, B., Grover, A., Nickel, M., Chen, R. T. Q., and Lipman, Y. Matching normalizing flows and probability paths on manifolds. *International Conference on Machine Learning*, 2022.
- Bose, J., Smofsky, A., Liao, R., Panangaden, P., and Hamilton, W. Latent variable modelling with hyperbolic normalizing flows. In III, H. D. and Singh, A. (eds.), *Proceedings of the 37th International Conference on Machine Learning*, volume 119 of *Proceedings of Machine Learning Research*, pp. 1045–1055. PMLR, 13–18 Jul 2020.
- Brakenridge, G. Global active archive of large flood events. <http://floodobservatory.colorado.edu/Archives/index.html>, 2017. Dartmouth Flood Observatory, University of Colorado,.
- Brehmer, J. and Cranmer, K. Flows for simultaneous manifold learning and density estimation. *Advances in Neural Information Processing Systems*, 33:442–453, 2020.
- Chen, R. T., Rubanova, Y., Bettencourt, J., and Duvenaud, D. K. Neural ordinary differential equations. *Advances in neural information processing systems*, 31, 2018.
- Chen, R. T. Q. torchdiffeq, 2018. URL <https://github.com/rtqichen/torchdiffeq>.
- Coifman, R. R. and Lafon, S. Diffusion maps. *Applied and computational harmonic analysis*, 21(1):5–30, 2006.
- Crane, K. 3D model repository. <https://www.cs.cmu.edu/~kmc Crane/Projects/ModelRepository/>.
- De Bortoli, V., Mathieu, E., Hutchinson, M., Thornton, J., Teh, Y. W., and Doucet, A. Riemannian score-based generative modeling. *Advances in Neural Information Processing Systems*, 2022.
- EOSDIS. Active fire data. <https://earthdata.nasa.gov/earth-observation-data/near-real-time/firms/active-fire-data>, 2020. Land, Atmosphere Near real-time Capability for EOS (LANCE) system operated by NASA’s Earth Science Data and Information System (ESDIS).
- Falcon, W. and team, T. P. L. Pytorch lightning, 2019. URL <https://github.com/Lightning-AI/lightning>.
- Falorsi, L. *Continuous normalizing flows on manifolds*. PhD thesis, University of Amsterdam, 2020.
- Gemici, M. C., Rezende, D., and Mohamed, S. Normalizing flows on riemannian manifolds. *arXiv preprint arXiv:1611.02304*, 2016.
- Herrera, P. Pyevtk, 2019. URL <https://github.com/paulo-herrera/PyEVTk>.
- Ho, J., Jain, A., and Abbeel, P. Denoising diffusion probabilistic models. *Advances in Neural Information Processing Systems*, 33:6840–6851, 2020.
- Horvat, C. and Pfister, J.-P. Denoising normalizing flow. *Advances in Neural Information Processing Systems*, 34: 9099–9111, 2021.
- Huang, C.-W., Aghajohari, M., Bose, A. J., Panangaden, P., and Courville, A. Riemannian diffusion models. *Advances in Neural Information Processing Systems*, 2022.
- Hunter, J. D. Matplotlib: A 2d graphics environment. *Computing in science & engineering*, 9(3):90, 2007.
- Hutchinson, M. A stochastic estimator of the trace of the influence matrix for Laplacian smoothing splines. 18: 1059–1076, 01 1989.
- Hyvärinen, A. and Dayan, P. Estimation of non-normalized statistical models by score matching. *Journal of Machine Learning Research*, 6(4), 2005.
- Jones, E., Oliphant, T., and Peterson, P. {SciPy}: Open source scientific tools for {Python}. 2014.

- Jones, P. W., Maggioni, M., and Schul, R. Manifold parametrizations by eigenfunctions of the laplacian and heat kernels. *Proceedings of the National Academy of Sciences*, 105(6):1803–1808, 2008.
- Jordahl, K., den Bossche, J. V., Fleischmann, M., Wasserman, J., McBride, J., Gerard, J., Tratner, J., Perry, M., Badaracco, A. G., Farmer, C., Hjelle, G. A., Snow, A. D., Cochran, M., Gillies, S., Culbertson, L., Bartos, M., Eubank, N., maxalbert, Bilogur, A., Rey, S., Ren, C., Arribas-Bel, D., Wasser, L., Wolf, L. J., Journois, M., Wilson, J., Greenhall, A., Holdgraf, C., Filipe, and Leblanc, F. *geopandas/geopandas: v0.8.1*, 2020.
- Kim, H., Lee, H., Kang, W. H., Lee, J. Y., and Kim, N. S. Softflow: Probabilistic framework for normalizing flow on manifolds. *Advances in Neural Information Processing Systems*, 33:16388–16397, 2020.
- Kloeden, P. E., Platen, E., and Schurz, H. Springer Science & Business Media, 2002.
- Kluyver, T., Ragan-Kelley, B., Pérez, F., Granger, B. E., Bussonnier, M., Frederic, J., Kelley, K., Hamrick, J. B., Grout, J., Corlay, S., et al. Jupyter notebooks-a publishing format for reproducible computational workflows. In *ELPUB*, pp. 87–90, 2016.
- Laboratory, S. U. C. G. The Stanford 3D scanning repository. <http://graphics.stanford.edu/data/3Dscanrep/>.
- Li, X., Wong, T.-K. L., Chen, R. T., and Duvenaud, D. Scalable gradients for stochastic differential equations. In *International Conference on Artificial Intelligence and Statistics*, pp. 3870–3882. PMLR, 2020.
- Lipman, Y., Rustamov, R. M., and Funkhouser, T. A. Biharmonic distance. *ACM Transactions on Graphics (TOG)*, 29(3):1–11, 2010.
- Lipman, Y., Chen, R. T., Ben-Hamu, H., Nickel, M., and Le, M. Flow matching for generative modeling. *International Conference on Learning Representations*, 2023.
- Liu, X., Gong, C., and Liu, Q. Flow straight and fast: Learning to generate and transfer data with rectified flow. *International Conference on Learning Representations*, 2023.
- Lou, A., Lim, D., Katsman, I., Huang, L., Jiang, Q., Lim, S. N., and De Sa, C. M. Neural manifold ordinary differential equations. *Advances in Neural Information Processing Systems*, 33:17548–17558, 2020.
- Lovell, S. C., Davis, I. W., Arendall III, W. B., De Bakker, P. I., Word, J. M., Prisant, M. G., Richardson, J. S., and Richardson, D. C. Structure validation by α geometry: ϕ , ψ and $c\beta$ deviation. *Proteins: Structure, Function, and Bioinformatics*, 50(3):437–450, 2003.
- Mathieu, E. and Nickel, M. Riemannian continuous normalizing flows. *Advances in Neural Information Processing Systems*, 33:2503–2515, 2020.
- McCann, R. J. Polar factorization of maps on riemannian manifolds. *Geometric & Functional Analysis GAFA*, 11(3):589–608, 2001.
- McKinney, W. *Python for data analysis: Data wrangling with Pandas, NumPy, and IPython*. ” O’Reilly Media, Inc.”, 2012.
- Murray, F. J. and Miller, K. S. *Existence theorems for ordinary differential equations*. Courier Corporation, 2013.
- Murray, L. J., Arendall III, W. B., Richardson, D. C., and Richardson, J. S. Rna backbone is rotameric. *Proceedings of the National Academy of Sciences*, 100(24):13904–13909, 2003.
- Neklyudov, K., Severo, D., and Makhzani, A. Action matching: A variational method for learning stochastic dynamics from samples. *arXiv preprint arXiv:2210.06662*, 2022.
- NOAA. Global significant earthquake database. <https://data.nodc.noaa.gov/cgi-bin/iso?id=gov.noaa.ngdc.mgg.hazards:G012153>, 2020a. National Geophysical Data Center / World Data Service (NGDC/WDS): NCEI/WDS Global Significant Earthquake Database. NOAA National Centers for Environmental Information.
- NOAA. Global significant volcanic eruptions database. <https://data.nodc.noaa.gov/cgi-bin/iso?id=gov.noaa.ngdc.mgg.hazards:G10147>, 2020b. National Geophysical Data Center / World Data Service (NGDC/WDS): NCEI/WDS Global Significant Volcanic Eruptions Database. NOAA National Centers for Environmental Information.
- Oliphant, T. E. *A guide to NumPy*, volume 1. Trelgol Publishing USA, 2006.
- Oliphant, T. E. Python for scientific computing. *Computing in Science & Engineering*, 9(3):10–20, 2007.
- Panozzo, D. and Jacobson, A. Libigl: A c++ library for geometry processing without a mesh data structure. 2014.
- Paszke, A., Gross, S., Massa, F., Lerer, A., Bradbury, J., Chanan, G., Killeen, T., Lin, Z., Gimelshein, N., Antiga, L., et al. Pytorch: An imperative style, high-performance deep learning library. In *Advances in neural information processing systems*, pp. 8026–8037, 2019.

- Polyak, B. T. and Juditsky, A. Acceleration of stochastic approximation by averaging. 1992.
- Ramachandran, P., Zoph, B., and Le, Q. V. Searching for activation functions. *arXiv preprint arXiv:1710.05941*, 2017.
- Rezende, D. J., Papamakarios, G., Racaniere, S., Albergio, M., Kanwar, G., Shanahan, P., and Cranmer, K. Normalizing flows on tori and spheres. In *International Conference on Machine Learning*, pp. 8083–8092. PMLR, 2020.
- Rozen, N., Grover, A., Nickel, M., and Lipman, Y. Moser flow: Divergence-based generative modeling on manifolds. *Advances in Neural Information Processing Systems*, 34:17669–17680, 2021.
- Skilling, J. The eigenvalues of mega-dimensional matrices. In *Maximum Entropy and Bayesian Methods*, pp. 455–466. Springer, 1989.
- Song, Y., Garg, S., Shi, J., and Ermon, S. Sliced score matching: A scalable approach to density and score estimation. In *Uncertainty in Artificial Intelligence*, pp. 574–584. PMLR, 2020a.
- Song, Y., Sohl-Dickstein, J., Kingma, D. P., Kumar, A., Ermon, S., and Poole, B. Score-based generative modeling through stochastic differential equations. *arXiv preprint arXiv:2011.13456*, 2020b.
- Van Der Walt, S., Colbert, S. C., and Varoquaux, G. The numpy array: a structure for efficient numerical computation. *Computing in Science & Engineering*, 13(2):22, 2011.
- Van Rossum, G. and Drake Jr, F. L. *Python reference manual*. Centrum voor Wiskunde en Informatica Amsterdam, 1995.
- Villani, C. *Optimal transport: old and new*, volume 338. Springer, 2009.
- Vincent, P. A connection between score matching and denoising autoencoders. *Neural computation*, 23(7):1661–1674, 2011.
- Waskom, M., Botvinnik, O., O’Kane, D., Hobson, P., Ostblom, J., Lukauskas, S., Gemperline, D. C., Augspurger, T., Halchenko, Y., Cole, J. B., Warmenhoven, J., de Ruiter, J., Pye, C., Hoyer, S., Vanderplas, J., Villalba, S., Kunter, G., Quintero, E., Bachant, P., Martin, M., Meyer, K., Miles, A., Ram, Y., Brunner, T., Yarkoni, T., Williams, M. L., Evans, C., Fitzgerald, C., Brian, and Qalieh, A. mwaskom/seaborn: v0.9.0 (july 2018), July 2018. URL <https://doi.org/10.5281/zenodo.1313201>.
- Yadan, O. Hydra - a framework for elegantly configuring complex applications. Github, 2019. URL <https://github.com/facebookresearch/hydra>.

A. Flow Matching Loss on manifolds

We provide the necessary derivations and proofs for the Conditional Flow Matching over a Riemannian manifolds; the proofs and derivations from (Lipman et al., 2023) are followed "as-is", with the necessary adaptation to the Riemannian setting.

Assumptions. We will use notations and setup from equation 2. Let $p(\cdot|x_1) : [0, 1] \rightarrow \mathfrak{P}$ be a (conditional) probability path sufficiently smooth with integrable derivatives, strictly positive $p_t(x|x_1) > 0$, and $p_0(x|x_1) = p$, where $p \in \mathfrak{P}$ is our source density. Let $u(\cdot|x_1) \in \mathfrak{U}$ be a (conditional) time-dependent vector field, sufficiently smooth with integrable derivatives and such that

$$\int_0^1 \int_{\mathcal{M}} |u_t(x|x_1)| p_t(x|x_1) d\text{vol}_x dt < \infty$$

Further assume $u_t(x|x_1)$ generates $p_t(x|x_1)$ from p in the sense of equation 2, i.e., if we denote by $\psi_t(x|x_1)$ the solution to the ODE (equation 1):

$$\frac{d}{dt} \psi_t(x|x_1) = u_t(\psi_t(x|x_1)|x_1) \quad (16)$$

$$\psi_0(x|x_1) = x \quad (17)$$

then

$$p_t(\cdot|x_1) = [\psi_t(\cdot|x_1)]_{\#} p \quad (18)$$

Proof of the marginal VF formula, equation 7. First, the Mass Conservation Formula Theorem (see, e.g., (Villani, 2009)) implies that $p_t(x|x_1)$ and $u_t(x|x_1)$ satisfy

$$\frac{d}{dt} p_t(x|x_1) + \text{div}(p_t(x|x_1) u_t(x|x_1)) = 0 \quad (19)$$

where div is the Riemannian divergence.

Next, we differentiate the marginal $p_t(x)$ w.r.t. t :

$$\begin{aligned} \frac{d}{dt} p_t(x) &= \int_{\mathcal{M}} \frac{d}{dt} p_t(x|x_1) q(x_1) d\text{vol}_{x_1} \\ &= -\text{div} \left[\int_{\mathcal{M}} u_t(x|x_1) p_t(x|x_1) q(x_1) d\text{vol}_{x_1} \right] \\ &= -\text{div} \left[p_t(x) \int_{\mathcal{M}} u_t(x|x_1) \frac{p_t(x|x_1) q(x_1)}{p_t(x)} d\text{vol}_{x_1} \right] \\ &= -\text{div} [p_t(x) u_t(x)] \end{aligned}$$

where in the first and second equalities we changed the order of differentiation and integration, and in the second equality we used the mass conservation formula for $u_t(x|x_1)$. In the previous to last equality we multiplied and divided by $p_t(x)$. In the last equality we defined the marginal vector field u_t as in equation 7.

RCFM loss equivalent to RFM loss. We will now show the equivalence of the RCFM loss (equation 8) and the RFM loss (equation 3). First note the losses expand as follows:

$$\begin{aligned} \mathcal{L}_{\text{RFM}}(\theta) &= \mathbb{E}_{t, p_t(x)} \|v_t(x) - u_t(x)\|_g^2 = \mathbb{E}_{t, p_t(x)} \|v_t(x)\|_g^2 - 2 \langle v_t(x), u_t(x) \rangle_g + \|u_t(x)\|_g^2 \\ \mathcal{L}_{\text{RCFM}}(\theta) &= \mathbb{E}_{\substack{t, q(x_1) \\ p_t(x|x_1)}} \|v_t(x) - u_t(x|x_1)\|_g^2 = \mathbb{E}_{\substack{t, q(x_1) \\ p_t(x|x_1)}} \|v_t(x)\|_g^2 - 2 \langle v_t(x), u_t(x|x_1) \rangle_g + \|u_t(x|x_1)\|_g^2 \end{aligned}$$

Second, note that

$$\begin{aligned}\mathbb{E}_{t,q(x_1),p_t(x|x_1)} \|v_t\|_g^2 &= \int_0^1 \int_{\mathcal{M}} \|v_t(x)\|_g^2 p_t(x|x_1) q(x_1) d\text{vol}_x d\text{vol}_{x_1} dt \\ &= \int_0^1 \int_{\mathcal{M}} \|v_t(x)\|_g^2 p_t(x) d\text{vol}_x dt \\ &= \mathbb{E}_{t,p_t(x)} \|v_t\|_g^2\end{aligned}$$

Lastly,

$$\begin{aligned}\mathbb{E}_{t,q(x_1),p_t(x|x_1)} \langle v_t(x), u_t(x|x_1) \rangle_g &= \int_0^1 \int_{\mathcal{M}} \langle v_t(x), u_t(x|x_1) \rangle_g p_t(x|x_1) q(x_1) d\text{vol}_x d\text{vol}_{x_1} dt \\ &= \int_0^1 \int_{\mathcal{M}} \left\langle v_t(x), \int_{\mathcal{M}} u_t(x|x_1) p_t(x|x_1) q(x_1) d\text{vol}_{x_1} \right\rangle_g d\text{vol}_x dt \\ &= \int_0^1 \int_{\mathcal{M}} \left\langle v_t(x), \int_{\mathcal{M}} u_t(x|x_1) \frac{p_t(x|x_1) q(x_1)}{p_t(x)} d\text{vol}_{x_1} \right\rangle_g p_t(x) d\text{vol}_x dt \\ &= \int_0^1 \int_{\mathcal{M}} \langle v_t(x), u_t(x) \rangle_g p_t(x) d\text{vol}_x dt \\ &= \mathbb{E}_{t,p_t(x)} \langle v_t(x), u_t(x) \rangle_g\end{aligned}$$

We got that $\mathcal{L}_{\text{RCFM}}(\theta)$ and $\mathcal{L}_{\text{RFM}}(\theta)$ differ by a constant,

$$\text{const} = \int_0^1 \int_{\mathcal{M}} \|u_t(x)\|_g^2 p_t(x) d\text{vol}_x dt - \int_0^1 \int_{\mathcal{M}} \|u_t(x|x_1)\|_g^2 p_t(x|x_1) q(x_1) d\text{vol}_x d\text{vol}_{x_1} dt$$

that does not depend on θ .

B. Proof of Proposition 3.2

Proposition 3.2. Consider a compact and smooth Riemannian manifold \mathcal{M} and metric g with geodesic distance $d_g(x, y)$. In case $k(x, y) = d_g(x, y)$ then $x_t = \psi_t(x|x_1)$ defined in equation 10 with the conditional VF in equation 11 is a geodesic connecting x_0 to x_1 .

Proof. First, note that by definition $\psi_0(x_0|x_1) = x_0$, and $\psi_1(x_0|x_1) = x_1$. Second, from Proposition 6 in McCann (2001) we have that

$$\nabla_x \frac{1}{2} d(x, y)^2 = -\log_x(y)$$

where \log is the Riemannian logarithm. From the chain rule we have

$$\nabla_x \frac{1}{2} d(x, y)^2 = d(x, y) \nabla_x d(x, y)$$

Since the logarithm map satisfies $\|\log_x(y)\|_g = d_g(x, y)$ we have that

$$\|\nabla d_g(x, y)\|_g = 1 \tag{20}$$

Furthermore, Proposition 3.1 with $k = d_g$ provides

$$d_g(x_t, x_1) = (1 - t) d_g(x_0, x_1) \tag{21}$$

Now, computing the length of the curve x_t (see equation 13) we get

$$\begin{aligned}
 \int_0^1 \|\dot{x}_t\|_g dt &= \int_0^1 \|u_t(x_t|x_1)\|_g dt \\
 &= \int_0^1 \left\| -\frac{d_g(x_t, x_1)}{1-t} \frac{\nabla d_g(x_t, x_1)}{\|\nabla d_g(x_t, x_1)\|_g^2} \right\|_g dt \\
 &= d_g(x_0, x_1) \int_0^1 \left\| \frac{\nabla d_g(x_t, x_1)}{\|\nabla d_g(x_t, x_1)\|_g^2} \right\|_g dt \\
 &= d_g(x_0, x_1) \int_0^1 dt \\
 &= d_g(x_0, x_1)
 \end{aligned}$$

where in the second equality we used the definition of the condition VF (equation 11), in the third equality we used equation 21, and in the fourth equality we used equation 20. Since x_t realizes a minimum of the length function, it is a geodesic. \square

C. Additional figures

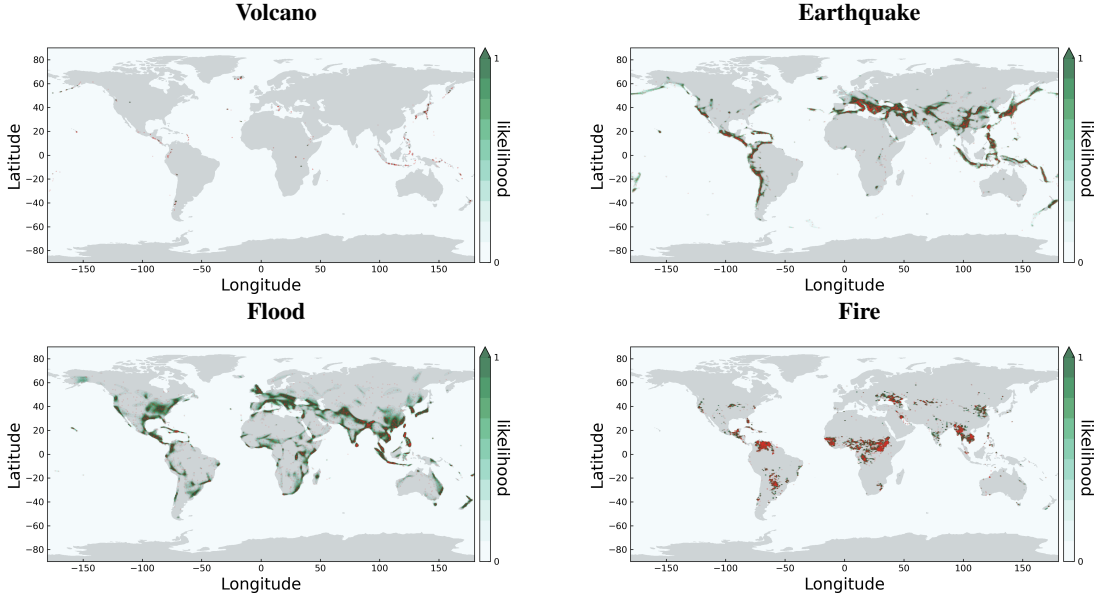


Figure 6: Data samples and Ramachandran plots depicting log likelihood for protein datasets.

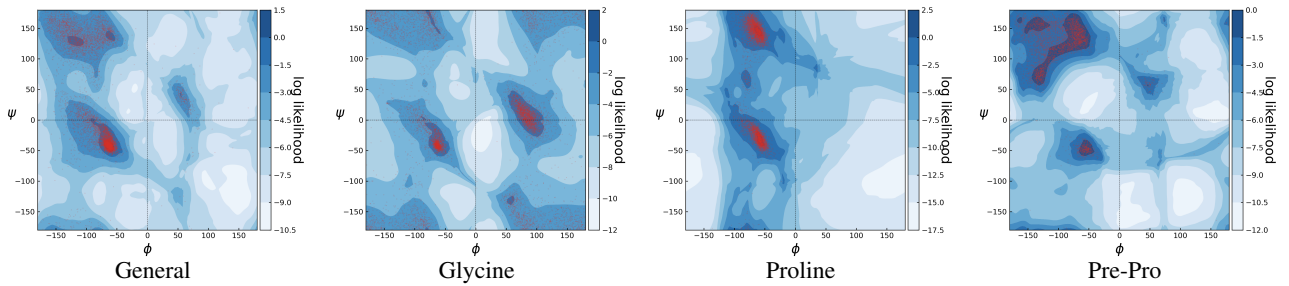


Figure 7: Data samples and Ramachandran plots depicting log likelihood for protein datasets.

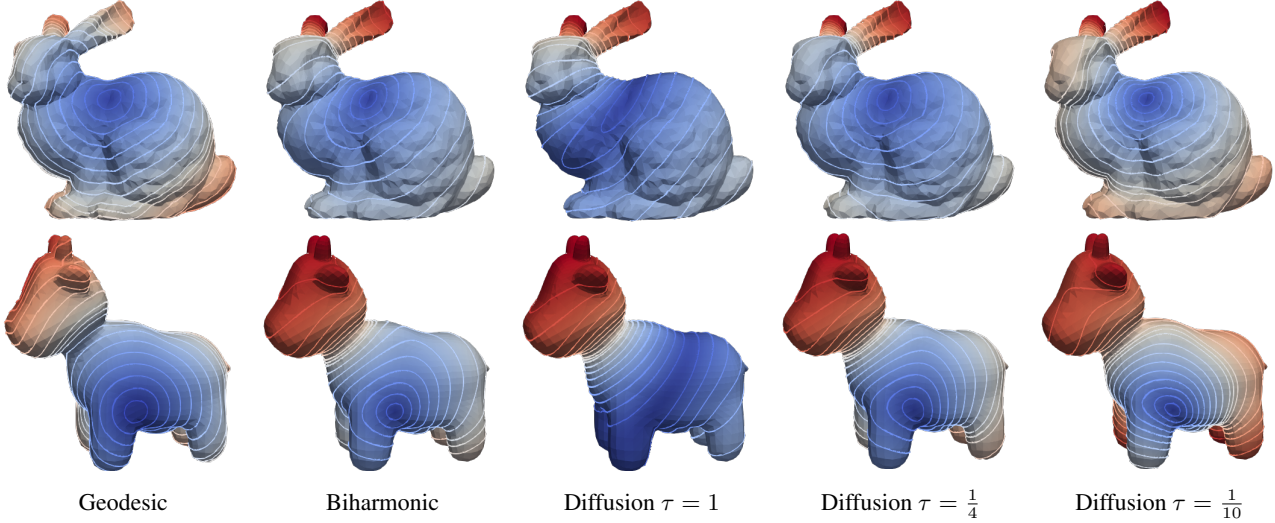


Figure 8: Contour plots of geodesic and spectral distances on general manifolds to a point on the manifold. The geodesic distance is expensive to compute and is non-smooth on general manifolds. The biharmonic distance behaves smoothly while the diffusion distance requires careful tuning of the hyperparameter τ .

D. Experiment Details

Training setup We tried our best to keep to the same training setup as prior works (Mathieu & Nickel, 2020; De Bortoli et al., 2022; Huang et al., 2022); however, as their exact data splits were not available, we used our own random splits. We followed their procedure and split the data according to 80% train, 10% val, and 10% test. We used seeds values of 0-4 for our five runs. We used the validation set for early stopping based on the validation NLL, and then only computed the test NLL using the checkpoint that achieved the best validation NLL. We used standard multilayer perceptron for parameterizing vector fields where time is concatenated as an input to the neural network. We generally used 512 hidden units and tuned the number of layers for each type of experiment, ranging from 6 to 12 layers. We used the Swish activation function (Ramachandran et al., 2017) with a learnable parameter. We used Adam with a learning rate of $1e-4$ and an exponential moving averaging on the weights (Polyak & Juditsky, 1992) with a decay of 0.999 for all of our experiments.

High-dimensional tori We use the same setup as De Bortoli et al. (2022). The data distribution is a wrapped Gaussian on the high-dimensional tori with a uniformly sampled mean and a scale of 0.2. We use a MLP with 3 hidden layers of size 512 to parameterize v_t , train for 50000 iterations with a batch size of 512. We then report the log-likelihood per dimension (in bits) on 20000 newly sampled data points.

Triangular meshes We use the exact open source mesh for Spot the Cow. For the Stanford Bunny, we downsample the mesh to 5000 triangles and work with this downsampled mesh. For constructing target distributions, we compute the eigenfunctions on a 3-times upsampled version of the mesh, threshold the k -th eigenfunction at zero, then normalized to construct the target distribution. This target distribution is uniform on each upsampled triangle, and further weighted by the area of each triangle. On the actual mesh we work with, this creates complex non-uniform distributions on each triangle. We also normalize the mesh so that points always lie in the range of $(-1, 1)$.

Maze manifolds We represent each maze manifold using triangular meshes in 2D. Each cell is represented using a mesh of 8×8 squares, with each square represented as two triangles. If two neighboring cells are connected, then we connect them using either 2×8 or 8×2 squares; if two neighboring cells are not connected (*i.e.* there is a wall), then we simply do not connect their meshes, resulting in boundaries on the manifold. This produces manifolds represented by triangular meshes where all the triangles are the same size. We randomly create maze structures based on a breadth-first-search algorithm, represent these using meshes, and we then normalize the mesh so that points lie in the range of $(0, 1)$.

Vector fields We parameterize vector fields as neural networks in the ambient space and project onto the tangent space at every x . That is, we model

$$v_t(x) = P_{\pi(x)} v_\theta(t, \pi(x)) \quad (22)$$

where π is the projection operator onto the manifold, *i.e.*

$$\pi(x) = \arg \min_{y \in \mathcal{M}} \|x - y\|_g, \quad (23)$$

and P_y is the orthogonal projection onto the tangent space at y .

Log-likelihood computation We solve for the log-density of a flow x_t with the vector field v_t by using the instantaneous change of variables (Chen et al., 2018), namely the integral

$$\frac{d}{dt} \log p_t(x_t) = -\text{div}_g(v_t), \quad (24)$$

where div_g is the Riemannian divergence and is equal to the Euclidean divergence in the ambient space when v_t is parameterized using equation 22 (Rozen et al., 2021, Lemma 2).

Numerical accuracy On the hypersphere, NLL values were computed using an adaptive step size ODE solver (`dopri5`) with tolerances of $1\text{e-}7$, and we always check that the solution did not leave the manifold. On the torus, we used the same solver but with tolerances of $1\text{e-}5$ as the ODE solver cannot leave the manifold. On general geometries represented using discrete triangular meshes, we used 1000 Euler steps with a projection after every step for evaluation (NLL computation and sampling after training). During training on general geometries, we solve for the path x_t using 300 Euler steps with projection after every step. In order to avoid division by zero, we solve x_t from $t = 0$ to $t = 1 - \varepsilon$, where ε is taken to be $1\text{e-}5$, which effectively flows the base distribution to a non-degenerate distribution around x_1 that approximates the Dirac distribution.